Experiments in Fluids (2005) 38: 759–769
DOI 10.1007/s00348-005-0959-7

ORIGINALS

William L. Keith · Kimberly M. Cipolla
David R. Hart · Deborah A. Furey

Drag measurements on long thin cylinders at small angles and high Reynolds numbers

Received: 27 October 2004 / Revised: 11 February 2005 / Accepted: 15 February 2005 / Published online: 20 April 2005

Abstract Measurements of the drag caused by turbulent boundary layer mean wall shear stress on cylinders at small angles of attack and high length Reynolds numbers ($8\times10^6 < Re_L < 6\times10^7$) are presented. The use of a full-scale, high-speed towing tank enabled the development of turbulent boundary layers on cylinders made of stainless steel, aluminum, titanium, and polyvinyl chloride. The diameter of all cylinders in this experiment was 12.7 mm; two cylinder lengths, 3.05 m and 6.10 m, were used, corresponding to aspect ratio values $L/a = 480$ and 960, respectively. Materials of various densities were towed at critical angles, resulting in linear cylinder geometry for tow speeds ranging from 2.6 m/s to 20.7 m/s and angles between 0° and 12°. Towing angles were measured with digital photography, and streamwise drag was measured with a strut-mounted load cell at the tow point. The measured tangential drag was very sensitive to small increases in angle at all tow speeds. A momentum thickness length scale is proposed to scale the tangential drag coefficient. The effects of the cross-flow resulting from the small angles of tow have a significant effect on the tangential drag coefficient values. A scaling for the orthogonal force on the cylinders was determined and provides a correction to published normal drag coefficient values for pure cross-flow. The presence of the axial turbulent boundary layer has a significant effect on these orthogonal forces.

W. L. Keith · K. M. Cipolla (✉) · D. R. Hart
Naval Sea Systems Command Newport,
1176 Howell Street, Newport,
RI 02841, USA
E-mail: cipollakm@npt.nuwc.navy.mil

D. A. Furey
Naval Sea Systems Command Carderock,
9500 MacArthur Blvd, West Bethesda,
MD 20817, USA

List of symbols

a	Cylinder radius (mm)
A_s	Total cylindrical surface area (m^2)
α	Cylinder angle of attack (°)
β, φ, γ	Coordinates in cross-sectional plane of cylinder
C_d	Tangential drag coefficient $= \frac{\bar{\tau}_w}{\frac{1}{2}\rho U_o^2}$
C_n	Orthogonal drag coefficient $= \frac{F\gamma}{\frac{1}{2}\rho (U_o \sin\alpha)^2 A_s}$
d	Cylinder diameter (mm)
δ	Maximum boundary layer thickness (mm)
F_x	Steady state (measured) horizontal force exerted by the fluid on the cylinder (N)
F_y	Steady state vertical force exerted by the fluid on the cylinder (N)
L	Cylinder length (m)
ν	Kinematic viscosity (m^2/s)
p	Static pressure (N/m^2)
P_β, P_γ	Pressure force components (N)
θ	Momentum thickness length scale (mm)
ρ	Fluid density (kg/m^3)
r	Radial coordinate (mm)
R_x, R_y	Reaction force components in moving coordinate system (N)
Re_D	Reynolds number based on diameter $= \frac{U_0 \sin(\alpha) d}{\nu}$
Re_L	Reynolds number based on length $= \frac{U_0 L}{\nu}$
Re_θ	Reynolds number based on momentum thickness length scale $= \frac{U_0 \theta}{\nu}$
S	Axial shear force (N)
σ	Circumferential wall shear stress (N/m^2)
T_β, T_γ	Circumferential wall shear force components (N)
τ_w	Local axial wall shear stress (N/m^2)
$\bar{\tau}_w$	Spatially averaged axial wall shear stress (N/m^2)
$u(r, \phi)$	Temporal mean streamwise velocity (m/s)
$\bar{u}(r)$	Circumferentially averaged streamwise velocity (m/s)
u_τ	Spatially averaged friction velocity $= \sqrt{\frac{\bar{\tau}_w}{\rho}}$ (m/s)
U_0	Tow speed (m/s)
W_{net}	Cylinder weight in water (N)

x, y Cartesian coordinates of moving reference frame (m)
ξ Coordinate along cylinder axis (m)

1 Introduction

Historically, the problem of turbulent boundary layers that develop on long, thin cylinders at small angles of attack has received much less attention than the analogous flat-plate problem. This problem relates directly to towed sonar arrays in turns, maneuvers and transient motions, and in cases where arrays experience positive or negative buoyancy in steady-state tows. Existing modeling and resulting real-time towed array shape predictions are limited in accuracy by the uncertainty in the orthogonal and tangential drag coefficient values. The turbulent wall pressure fluctuations, as well as the flow-induced cylinder vibrations for this class of flows, are also of primary importance with regard to the self-noise of towed array sonar systems. Willmarth et al. (1977) and Bull and Dekkers (1993) suggested that significant effects on the turbulent boundary layer structure may occur because of very small angles of attack. This sensitivity to small angles led Willmarth et al. (1976) to design a vertical wind tunnel to eliminate cylinder static deflections caused by gravity. In addition, for very long cylinders, the ratio δ/a becomes large such that differences between the axisymmetric boundary layer and a hypothetical flat-plate case become more pronounced, as discussed by Lueptow (1988). Bucker and Lueptow (1998) utilized a vertical wind tunnel to make velocity measurements on cylinders at very small angles ($\pm 0.55°$). Snarski (2004) measured wall pressure fluctuations on short cylinders at yaw angles varying from 0° to 90° in 15° increments. However, the problem of interest here is a long cylinder at small angles and very high Reynolds numbers, which has not been investigated by previous researchers.

Measurements by Cipolla and Keith (2003a, 2003b) for which $\delta/a > 100$ and $L/a > 10{,}000$, and Reynolds numbers of $10^4 < Re_\theta < 10^5$ and $10^8 < Re_L < 10^9$ established that the wall shear stress is significantly higher and the spatial growth of the boundary layers is lower than that for a comparable flat-plate case. Also, the mean wall shear stress exhibited spatial variations not seen in zero-pressure-gradient flat-plate turbulent boundary layers. The length scales of these variations are three orders of magnitude larger than the maximum momentum thickness at the end of the line. The effect was found for towing speeds of 3.1 m/s, 9.3 m/s, and 14.4 m/s, with the minimum shear stress occurring at approximately the same streamwise distance (90 m) for each tow speed. These results suggest that a length scale on the order of 100δ exists to observe this effect. Furthermore, ongoing stereo particle image velocimetry (PIV) measurements by Furey et al. (2004) for towed lines of the same diameter reveal a decrease in the boundary layer thickness to a minimum value at the same location (90 m) as the minimum in the shear stress. The apparent quasi-periodic behavior in both δ and $\bar{\tau}_w$ has never been experimentally observed before. In each of these investigations, the tow angle was less than 1°. These results, in part, motivated the present investigation aimed at measuring the sensitivity of the flow field to small angles.

In this investigation, the problem of a long, thin cylinder at small angles to the flow at moderate-to-high Reynolds numbers is considered. This geometry has several applications in which the total drag in the direction of tow is a primary measured quantity. The analysis includes calculating the force along the axis of the cylinder, which is a primary design parameter for towed arrays. The force orthogonal to the cylinder axis is also calculated, and a scaling that accounts for the effect of the turbulent boundary layer on this orthogonal force is presented.

The use of a high-speed towing tank generates length Reynolds numbers and ratios of the outer to inner boundary layer length scales that are directly relevant to undersea towed array applications. This investigation required L/a to be on the order of 100 and required the length to be large in comparison to the relevant turbulent length scales generated. A direct measurement of the total drag on long, small-diameter cylinders enables very accurate measurements of the spatially averaged mean wall shear stress. This measurement, combined with measurements of the cylinder angle, leads to a relationship among the measured drag, axial shear force, orthogonal force, cylinder angle, and tow speed. A control volume analysis was used to determine a momentum thickness length scale θ at the end of the cylinder from the axial force. The use of flush-mounted hot film sensors was considered but deemed impractical due to difficulties in calibration, as discussed by Colella and Keith (2003) and Keith and Bennett (1991). A digital particle image velocimetry (DPIV) system has since been developed for this facility (Furey et al. 2004) and enables turbulence measurements to be obtained for these class of flows.

2 Description of experiments

2.1 Experimental facility

Towing tests were conducted using carriage number 5 at the Naval Sea Systems Command (NAVSEA) Carderock high-speed towing basin (see Schoenherr and Brownell (1963) or go to http://www50.dt.navy.mil/facilities/data/carr5.html for the specifications of this facility). The high-speed basin, which is 904 m long, comprises two adjoining sections: (1) a deep-water section that is 4.9 m deep, 514 m long, and 6.4 m wide; and

(2) a shallow-water section that is 3 m deep, 356 m long, and 6.4 m wide.

The carriage is propelled by 16 weight-bearing vertical drive wheels and 16 horizontal driving guide wheels. The speed is regulated with an adjustable direct current voltage automatic feedback computerized control system. An automatic controller maintains the carriage speed to within ± 0.03 m/s. The maximum carriage speed is 25.7 m/s (50 knots), and the maximum average acceleration rate is 0.49 m/s^2. Additionally, wave-absorber troughs, which dampen standing surface waves generated by the tow strut, extend along the sidewalls of the tow tank. The fresh water in the tank was at a uniform temperature of 20.6°C, with a kinematic viscosity of 1.01×10^{-6} m^2/s and a density of 998 kg/m^3. No measurable change in the water density and salinity was obseved throughout the depth and length of the tank over the duration of the experiments.

2.2 Test setup

The test setup was configured for towing cylinders ($L=3.05$ m and 6.10 m, $a=6.35$ mm) at critical angles over a range of speeds in a straight-tow configuration, with a simple pinned connection at the tow point. Critical angles of tow occur when a body under tow is allowed to reach an equilibrium position with no applied torque at the tow point. For a particular tow speed, variations in the angle were achieved by interchanging cylinders of different densities. This setup, shown in Fig. 1, eliminated the need for support at the trailing edge, which would cause additional unknown drag forces applied to the load cell. This design also leads to a zero-bending moment at the tow point and load cell, and minimizes bending along the length of the cylinder. A cutaway view of the tow point inside the fairing is shown in Fig. 2.

The load cell was attached to the base of the towing strut, and a linear bearing was used to support a connecting rod between the load cell and the connecting pin. The fixture was designed to minimize transmission of any vertical force to the load cell and was enclosed in a fiberglass fairing to minimize the generation of turbulence. The fairing, which has a rounded nose and flat sides, is approximately 35.6 cm long, 7.6 cm wide, and 15.2 cm high. The shape of the fairing was designed to maximize the internal volume while minimizing form drag (Fellman and Johnston 1991). For each time series of load cell data, the mean value was calculated while the carriage speed was at steady state. At most tow speeds, the typical record length was greater than 30 s and consisted of 50–100 samples. At the higher tow speeds, the typical record length was 15 s and approximately 40 samples. The experiment was not designed to obtain meaningful rms or spectral measurements from the drag data, as evidenced by the low sample rates used. The normalized random error was within 2% for all steady-state load cell measurement records. This ensemble-averaged force F_x represents the spatially integrated component of force in the tow direction over the surface of the cylinder. For small angles, this force is dominated by the streamwise component of the mean wall shear stress, with an additional component caused by the pressure and circumferential shear forces on the cylinder surface. Because of the large aspect ratios $L/a=480$ and 960, the effects of cylinder base drag were negligible. This result was verified experimentally by repeating drag measurements with and without two different tail cones attached to the cylinder trailing edge. The tail cones were right circular cones with diameters of 12.7 mm and lengths of 76.2 mm and 38.1 mm, respectively. The presence of either cone caused no increase in measured drag with respect to the blunt end case. For each combination of tow speed and tow angle, multiple runs were performed to demonstrate repeatability.

Cylinder tow angles were measured using a Dantec HiSense digital camera, with an 8-bit resolution and a 1280×1024-pixel, 60-mm lens. The camera was located in a photography pit, 488-m down the tow tank. It was determined from the digital photographs that all cylinders towed in a linear configuration, with a standard error of less than 5%. The matrix of completed test runs is given in Table 1, which lists the cylinder material used to achieve each combination of tow angle and speed. In all cases, the cylinders towed in a linear configuration with no measurable mean deformation along the axis.

2.3 Test methodology

2.3.1 *Fluid forces*

In addition to the two measured quantities F_x and α, the fluid forces acting on the cylinder caused by the turbulent flow field are depicted in Fig. 3. As shown, these forces are considered to be steady-state values averaged over the length of the cylinder; the tow direction is left to

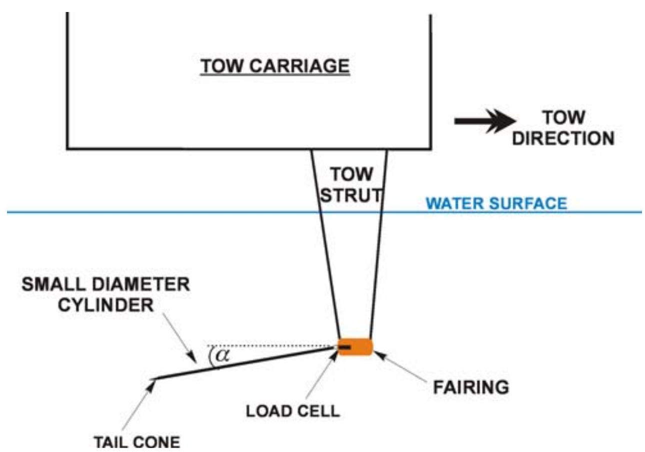

Fig. 1 Schematic of the towing configuration

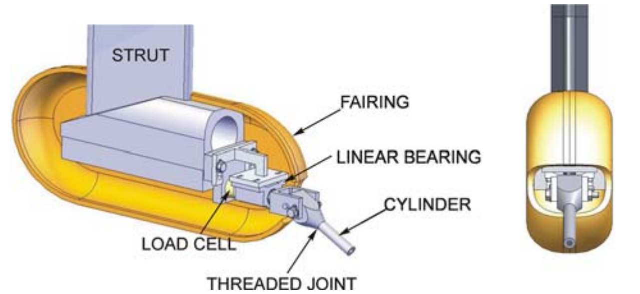

Fig. 2 Solid model cross section and end view of the tow point design

right. The resultant forces are placed at the center of mass of the cylinder, which assumes that the forces are uniformly distributed along the axis of the cylinder. This assumption is consistent with a negligible pressure gradient in a direction parallel to the cylinder axis (at any radial location on the cylinder surface), and is supported by the measured linearity of the cylinders under tow. The x–y coordinate system is moving at a constant velocity equal to the tow speed. Because the cylinder is towed in a critical angle configuration with a pinned connection at B, the moment about B, $M_B=0$.

The objective of the following analysis was to develop an expression for the fundamental boundary layer parameters $\bar{\tau}_w$ and θ in terms of the measured drag and angle. Figure 4 is a cross-sectional view of the cylinder, normal to the cylinder axis, showing the pressure and circumferential shear stress in that plane.

Considering the forces in the β–γ plane, the components of the pressure force are:

$$P_\beta = \int_0^{2\pi}\int_0^{L} p(\phi)a\cos\phi\,\mathrm{d}\phi\,\mathrm{d}\xi \tag{1}$$

and:

$$P_\gamma = \int_0^{2\pi}\int_0^{L} p(\phi)a\sin\phi\,\mathrm{d}\phi\,\mathrm{d}\xi \tag{2}$$

The circumferential wall shear stress also yields force components in the β direction and γ direction:

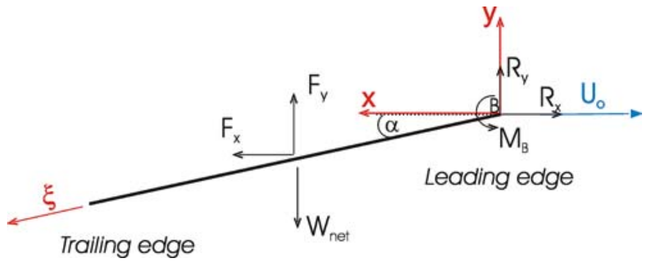

Fig. 3 Free body diagram of a cylinder towed in a critical angle configuration

$$T_\beta = \int_0^{2\pi}\int_0^{L} \sigma(\phi)a\sin\phi\,\mathrm{d}\phi\,\mathrm{d}\xi \tag{3}$$

and:

$$T_\gamma = \int_0^{2\pi}\int_0^{L} \sigma(\phi)a\cos\phi\,\mathrm{d}\phi\,\mathrm{d}\xi \tag{4}$$

Because of the symmetry of the flow (zero yaw angle), $P_\beta=0$ and $T_\beta=0$. The forces P_γ and T_γ contribute to the x component and y component of force shown in Fig. 3. The force attributed to the wall shear stress in the axial direction is:

$$S = \int_0^{2\pi}\int_0^{L} \tau_w(\phi,\xi)a\,\mathrm{d}\phi\,\mathrm{d}\xi \tag{5}$$

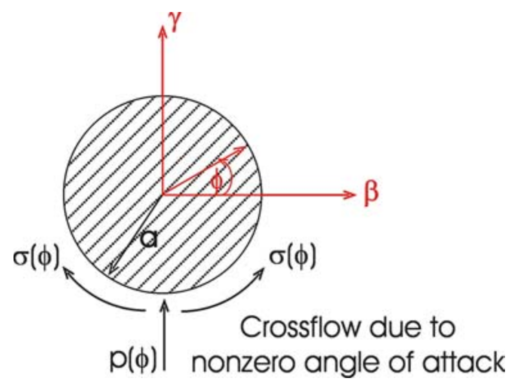

Fig. 4 Cross-sectional view of cylinder

Table 1 Tow angles versus tow speeds for the materials tested

Speed (m/s)	Measured angle (degrees)														
	1.5	2	2.5	3	3.5	4	5	5.5	6	6.5	7	8	9	11	11.5
2.6									PVC						
5.2				PVC							AL		Ti		
6.2										AL		Ti			SS
7.8		PVC					AL				Ti			SS	
10.4		PVC			AL			Ti				SS			
12.9			AL			Ti				SS					
15.5	PVC		AL	Ti			SS								
18.1			Ti			SS									
20.7		Ti													

SS = Stainless steel. *AL* = Aluminum. *Ti* = Titanium. *PVC* = Polyvinyl chloride. All data for cylinder length 3.05 m

The forces given in Eqs. 2, 4, and 5 are components of the total horizontal and vertical fluid forces acting on the cylinder:

$$F_x = P_\gamma \sin\alpha + T_\gamma \sin\alpha + S\cos\alpha \tag{6}$$

and:

$$F_y = P_\gamma \cos\alpha + T_\gamma \cos\alpha - S\sin\alpha \tag{7}$$

Static equilibrium defines the reaction forces at the tow point as:

$$F_x = R_x \tag{8}$$

and:

$$W_{\mathrm{net}} - F_y = R_y \tag{9}$$

Summing the moments about the tow point B, and assuming a frictionless pin, yields:

$$\sum M_{\mathrm{B}} = 0 = F_y \frac{L}{2}\cos\alpha + F_x \frac{L}{2}\sin\alpha - W_{\mathrm{net}}\frac{L}{2}\cos\alpha \tag{10}$$

Equation 10 simplifies to the following equation:

$$F_y = \frac{W_{\mathrm{net}}\cos\alpha - F_x\sin\alpha}{\cos\alpha} = W_{\mathrm{net}} - F_x\tan\alpha \tag{11}$$

Note that all the quantities on the right side of Eq. 11 are measured. Combining Eqs. 7 and 11, and using Eq. 6 to eliminate $(P_\gamma + T_\gamma)$, gives the following expression for the axial wall shear force:

$$S = \frac{F_x}{\cos\alpha} - W_{\mathrm{net}}\sin\alpha \tag{12}$$

The following expressions for the spatially averaged axial wall shear stress and tangential drag coefficient follow immediately from Eq. 12:

$$\bar{\tau}_{\mathrm{w}} = \frac{S}{A_{\mathrm{s}}} \tag{13}$$

and:

$$C_{\mathrm{d}} = \frac{\bar{\tau}_{\mathrm{w}}}{\frac{1}{2}\rho U_0^2} \tag{14}$$

This formulation, which gives the shear force tangential to the cylinder, is most relevant to the case of a cylindrical turbulent boundary layer and enables the calculation of the momentum thickness from a control volume analysis, which is analogous to what is stated by Cipolla and Keith (2003a) and is described in Sect. 2.3.2. The total force exerted by the fluid on the cylinder orthogonal to the cylinder axis is composed of the pressure and the circumferential shear forces in the γ direction:

$$F_\gamma = P_\gamma + T_\gamma \tag{15}$$

Combining Eqs. 7 and 11 leads to an expression for $(P_\gamma + T_\gamma)$:

$$F_\gamma = P_\gamma + T_\gamma = W_{\mathrm{net}}\cos\alpha \tag{16}$$

An orthogonal drag coefficient can then be defined as:

$$C_{\mathrm{n}} = \frac{F_\gamma}{\frac{1}{2}\rho(U_0\sin\alpha)^2 A_{\mathrm{s}}} \tag{17}$$

Note that this coefficient uses the relevant component of velocity, $U_0\sin\alpha$, to non-dimensionalize the force.

2.3.2 *Momentum thickness length scale*

From the outset, it is assumed that an outer length scale will be required to scale the data in this investigation. Cebeci and Smith (1974) derive an expression for the momentum thickness on a body of revolution. Following Cipolla and Keith (2003a, 2003b), a control volume analysis is utilized to determine a momentum thickness length scale θ at the end of the towed cylinders from the measured drag force. In Fig. 5, a cylindrical control volume is defined so that the outer edge is the maximum boundary layer thickness at the end of the cylinder. The axis of the control volume is coincident with the axis of the cylinder, that is, the ξ axis. For the non-zero tow angles considered here, the boundary layer properties are not symmetric and vary with φ.

When considering the forces on the control volume in the axial ξ direction, the only surface force S is the shear force acting on the wall of the cylinder. Control surfaces 1 and 2 (Fig. 5) experience different static pressure forces caused by the differences in elevation. This pressure differential is balanced by the component of the net weight in that direction, so that the net body force F_{B} is zero. For the case of steady-state flow, the governing equations (conservation of mass and momentum) are:

$$\int_{\mathrm{CS}} \rho\bar{V}\cdot \mathrm{d}\bar{A} = 0 \tag{18}$$

and:

$$\int_{\mathrm{CS}} (u(r,\phi)\cos\alpha)\rho\bar{V}\cdot \mathrm{d}\bar{A} = S \tag{19}$$

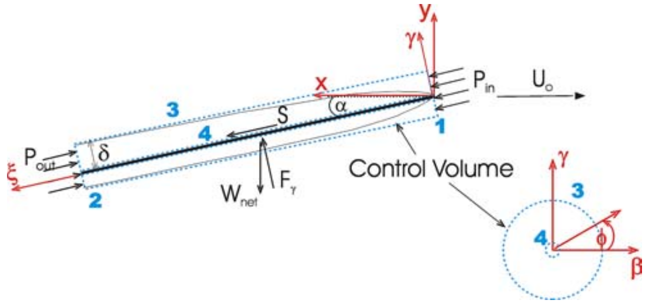

Fig. 5 Control volume for a cylinder at an angle to the tow direction

Let $u(r, \varphi)$ be the horizontal velocity in the boundary layer at the end of the cylinder. Then, defining:

$$\bar{u}(r) = \frac{1}{2}\pi \int_0^{2\pi} u(r, \phi)\mathrm{d}\phi \tag{20}$$

establishes $\bar{u}(r)$ as a circumferentially averaged velocity component.

Because the tow direction is at an angle α to the cylinder axis, the velocity at the inlet to the control volume is $U_0 \cos \alpha$. There is no flow across control surface 4 (see inset of cross-section in Fig. 5), and evaluating Eq. 18 gives:

$$2\pi \cos \alpha \int_a^{a+\delta} (U_0 - \bar{u}(r))r\mathrm{d}r = (\bar{V} \cdot \bar{A})_3 \tag{21}$$

Using Eq. 21, Eq. 19 becomes:

$$\frac{S}{\rho(U_0 \cos \alpha)^2} = \int_0^{2\pi} \int_a^{a+\delta} \left[\frac{\bar{u}(r)}{U_0}\left(1 - \frac{\bar{u}(r)}{U_0}\right)\right] r\mathrm{d}r\mathrm{d}\phi \tag{22}$$

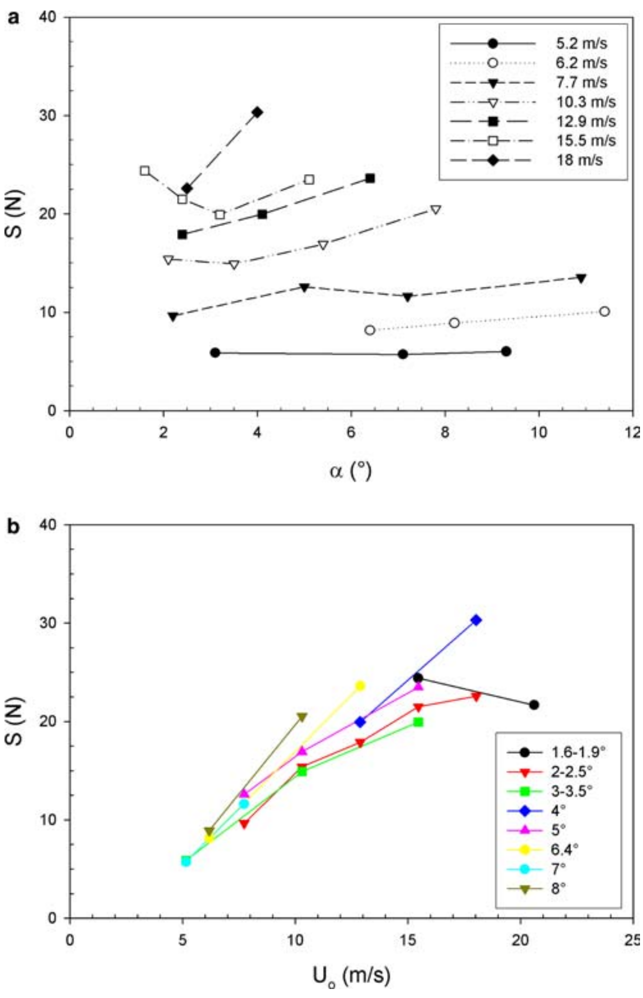

Fig. 6 **a** Shear force versus tow angle ($L = 3.05$ m). **b** Shear force versus tow speed ($L = 3.05$ m)

where $\bar{u}(r)$ is defined by Eq. 20. This immediately simplifies to:

$$\frac{S}{\rho(U_0 \cos \alpha)^2} = 2\pi \int_a^{a+\delta} \left[\frac{\bar{u}(r)}{U_0}\left(1 - \frac{\bar{u}(r)}{U_0}\right)\right] r\mathrm{d}r \tag{23}$$

For a cylindrical geometry and axisymmetric boundary layer, the definition of momentum thickness, as given by White (1969), following the work of Kelly (1954), is:

$$\theta^2 + 2a\theta = 2\int_a^{a+\delta} \left[\frac{\bar{u}(r)}{U_0}\left(1 - \frac{\bar{u}(r)}{U_0}\right)\right] r\mathrm{d}r \tag{24}$$

Equating the right sides of Eqs. 23 and 24, and then simplifying, yields:

$$\frac{S}{\pi\rho(U_0 \cos \alpha)^2} = \theta^2 + 2a\theta \tag{25}$$

Since the left side of Eq. 25 consists of measured quantities, this expression enables the evaluation of a momentum thickness length scale θ at the end of the cylinder. Given that the velocity $\bar{u}(r)$ in Eq. 24 is a circumferentially averaged value, θ is necessarily a circumferentially averaged length scale.

3 Results of experiments

3.1 Wall shear force and momentum thickness

The measured data were used to calculate the axial wall shear force S for the four 3.05-m cylinders. Figure 6a, b shows the data plotted as S versus α for constant speeds and S versus U_0 for constant angles of attack. As expected, the shear force for a fixed angle increased with tow speed; however, no clear trend was observed when the angle was varied at a fixed speed.

The axial wall shear stress $\bar{\tau}_w$ and the tangential drag coefficient C_d were calculated from the shear force S using Eqs. 13 and 14. In defining C_d, the tow speed U_0, rather than the axial component $U_0 \cos \alpha$, was used. For reference, Fig. 7 shows $\bar{\tau}_w$ versus α for all combinations of tow speed and angle. The different colors denote angles that are similar, and the symbols denote equivalent tow speeds.

Non-dimensionalizing $\bar{\tau}_w$ to obtain C_d, as shown in Fig. 8, leads to a clear trend of decreasing values of C_d with increasing speed over the range of angles. Each data set is for constant speed, except for the data obtained with the 6.10-m long cylinder, which was towed at three different speeds. A significant variation in C_d with angle was measured, and also depended strongly on the value of U_0. Also, at a given speed, C_d increases with increasing angle. Viewing C_d as a function of angle is not expected to collapse the data since α is not a scaled quantity.

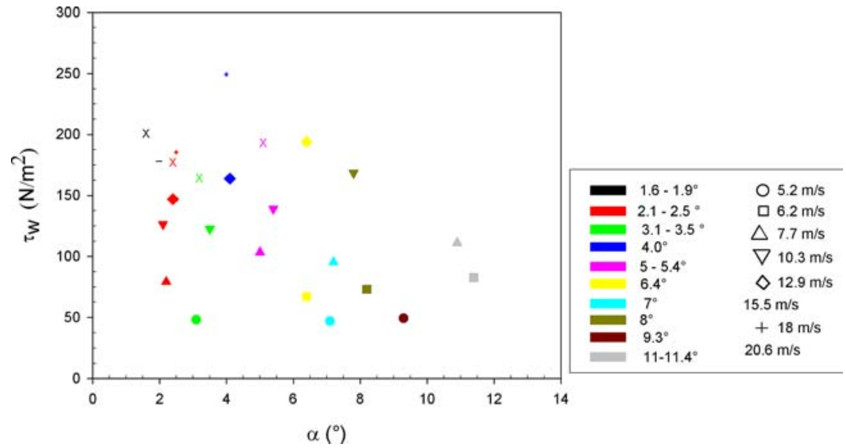

Fig. 7 Mean wall shear stress versus tow angle ($L = 3.05$ m)

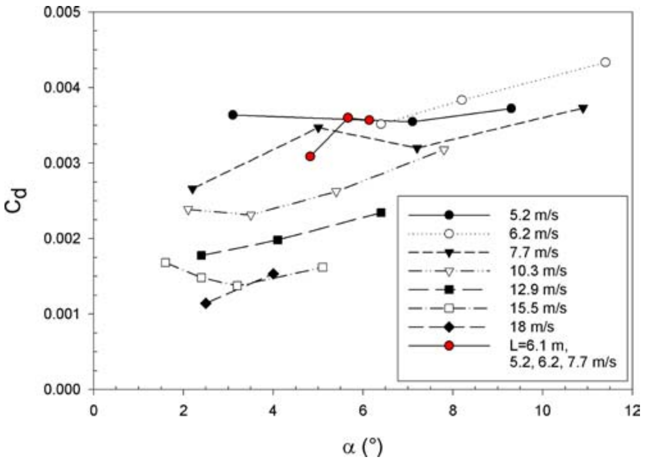

Fig. 8 Tangential drag coefficient versus tow angle

The momentum thickness length scales θ were calculated using Eq. 25 and are shown as a function of tow angle in Fig. 9. The trends of increasing θ with decreasing tow speed and increasing angle are apparent. In addition, the 6.1-m data shows the significant increase in θ with respect to the 3.05-m data. In order to improve the collapse of the data in Fig. 8, the length scale θ is introduced through the non-dimensional quantity $(L/\theta)^n$, where n is an empirically determined constant. The ratio L/θ can be viewed as a metric of boundary layer growth over the length of the cylinder, for sufficiently small angles. The results of this scaling are shown in Fig. 10, where both the 3.05-m and 6.10-m data are included; $n = 0.5$ was found to provide the best collapse. The scaling reduces the scatter of the drag coefficient data. However, note that α represents a single parameter rather than a scaled quantity. Therefore, a tight collapse of the data in this form is not expected.

The results shown in Fig. 11 are for data sets of approximately constant values of angle of attack, with C_d plotted as a function of U_0 for all angles obtained for the 3.05-m and 6.1-m long cylinders. The dominant trend of decreasing C_d with increasing speed for all angles is evident, with the additional effect that the largest angles correspond to higher values of C_d. The drag coefficient predicted for a 3.05-m flat plate from Schlichting (1979, p. 639) is plotted as a dashed line. The C_d values are lower than those that flat-plate theories predict at speeds greater than approximately 13 m/s, regardless of angle. The fact that the values for the two cylinder lengths match demonstrates that the measurements are not sensitive to the experimental setup and

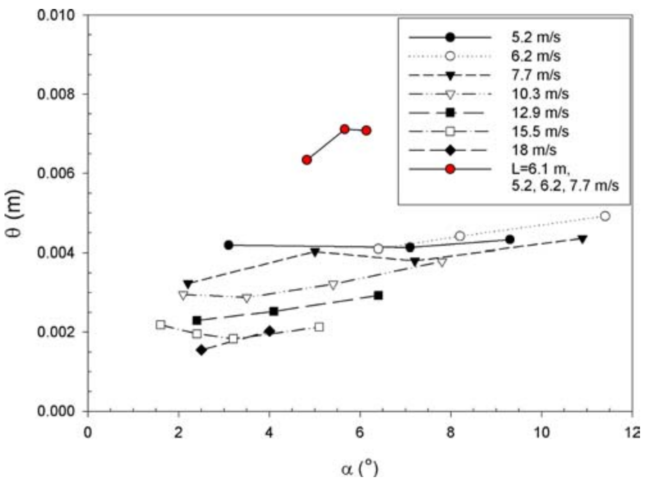

Fig. 9 Momentum thickness length scale versus tow angle

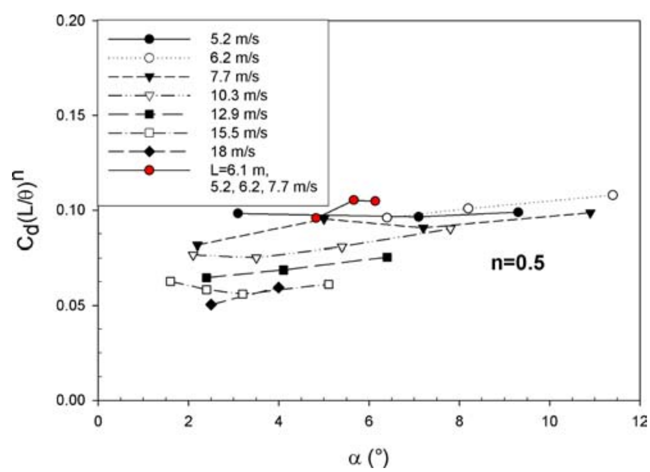

Fig. 10 Non-dimensional scaling for drag coefficient

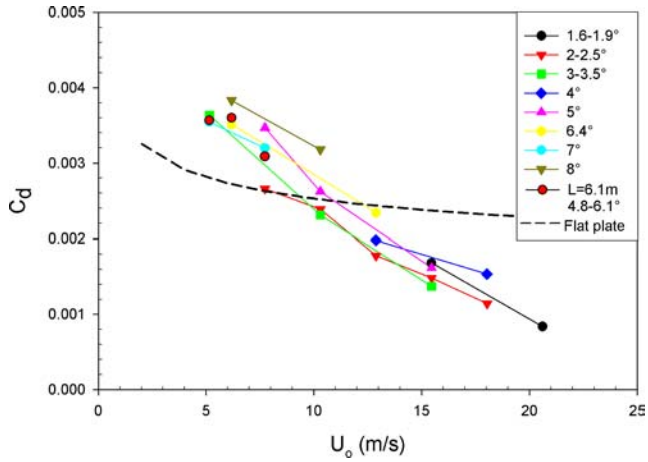

Fig. 11 Tangential drag coefficient versus tow speed ($L = 3.05$ m)

that an equilibrium flow field exists. Based on the experimental method, the uncertainty in the angle is estimated to be $\pm 0.5°$. For example, at $U_0 = 15.5$ m/s, an increase in C_d from 0.0014 to 0.0017 occurs over a range of angles between 1.6° and 5°. At $U_0 = 10.3$ m/s, an increase in C_d from 0.0023 to 0.0032 (50% increase) occurs over a range of angles between 2° and 8°.

Figure 12 displays u_τ/U_0 as a function of Re_L, with data from Coles (1953) for an ideal flat-plate boundary layer shown as a solid blue line. The quantity u_τ/U_0 decreases with increasing length Reynolds number for both the cylinder and the flat-plate data. The cylinder data highlight the variation of shear stress with small changes in angle at all speeds. In addition, the decrease in u_τ/U_0 with Re_L is more rapid than the flat-plate case. This formulation does not lead to a tight collapse of the data for the two different cylinder lengths at comparable angles, and points to the need for an outer length scale rather than simply Re_L to obtain a better collapse.

The ratio of outer-length scale to inner-length scale values $\theta/(v/u_\tau)$ is plotted as a function of the momentum thickness length scale Reynolds number Re_θ in Fig. 13, along with values for a flat-plate boundary layer taken from Coles (1953). No clear trend is apparent with speed or angle, but the data is distributed around the flat-plate results. Measurements obtained for higher aspect ratio cylinders (Cipolla and Keith 2003a, 2003b; Furey et al. 2004) showed values of $\theta/(v/u_\tau)$ that were two to three times higher than flat-plate values in this range of Reynolds numbers. Assuming that the length scale δ is an order of magnitude greater than θ (which holds for flat-plate equilibrium boundary layers), the ratio δ/d would be of order 1 here. This is sufficient for mild but not strong curvature effects. Therefore, the differences in the ratio of outer to inner length scales with respect to the flat-plate case are primarily due to the effects of the towing angle, since even the smallest angles differ from the flat-plate case.

Figure 14 shows $\bar{\tau}_w$ versus length Reynolds number Re_L for all combinations of tow speed and angle for the 3.05-m cylinders. Also plotted as open circles are the values of the spatially averaged $\bar{\tau}_w$ predicted for a flat-plate turbulent boundary layer (Schlichting 1979) of the same length at zero angle of attack. Consideration of the variation of $\bar{\tau}_w$ as a function of $U_0\ L/v$ facilitates comparison of the measured data with flat-plate boundary layer results. The length scale L can be viewed as a reference length (since data for only $L = 3.05$ m is included here) and increasing values of $U_0\ L/v$ are strictly the result of an increase in tow speed. At low speeds, the values of $\bar{\tau}_w$ agree with flat-plate values; however, as U_0 is increased, $\bar{\tau}_w$ appears to reach a maximum value and departs significantly from the flat-plate values. This result corresponds to the lower C_d values shown in Fig. 11 at high speeds. This trend in $\bar{\tau}_w$ seems to depend more strongly on tow speed and less on particular angles.

Considering the results of Fig. 13, it can be assumed that a hairpin vortex structure exists in the near-wall turbulence field, which is qualitatively similar to the flat-plate boundary layer case. For a flat-plate boundary layer, as U_0 increases, the wall shear stress increases and the hairpin vortex diameters and spacing decrease. For the cases investigated here, the hairpin diameter and spacing reached a minimum and then increased as U_0 increased. Assuming an average hairpin diameter of 10 viscous lengths, and an average spacing of 100 viscous lengths (Hinze 1975), the maximum number of hairpin pairs around the circumference of the cylinder is 200, based on the maximum value of $\bar{\tau}_w$. Because the hairpin spacing is two orders of magnitude smaller than the

Fig. 12 Non-dimensional friction velocity versus length Reynolds number

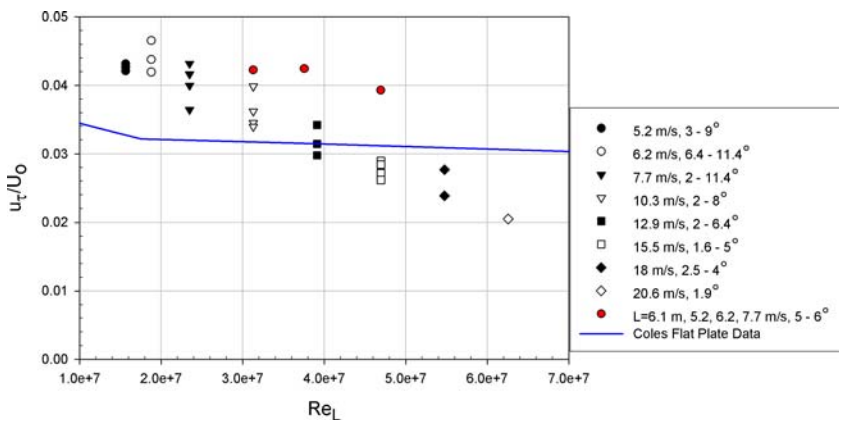

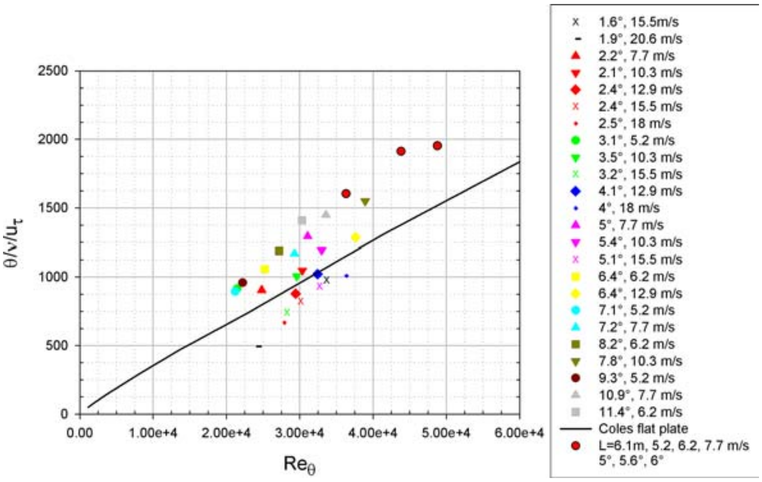

Fig. 13 Ratio of outer to inner-length scales versus momentum Reynolds number

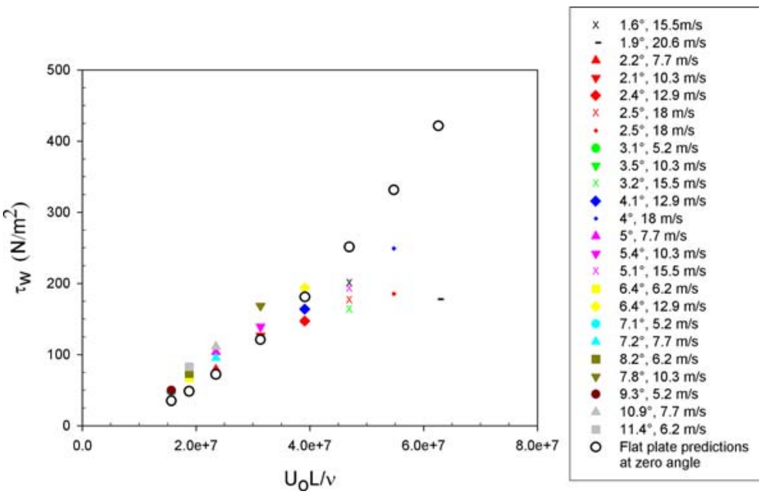

Fig. 14 Mean wall shear stress versus length Reynolds number ($L = 3.05$ m)

diameter of the cylinder, the effects of transverse curvature are expected to be small. Therefore, the dominant effect is likely to be the cross-flow component caused by the non-zero angle of attack. Additional experiments in which the cylinder diameter is varied would clarify whether the value of 200 hairpin pairs is, in fact, a meaningful constant. Detailed turbulence measurements would reveal whether the flat-plate assumption of hairpin spacing is valid, or whether the entire structure changes for this class of boundary layers.

3.2 Orthogonal force

The orthogonal drag coefficient C_n was calculated from the orthogonal force using Eq. 17. Figure 15, which is a plot of C_n versus Re_D for the 3.05-m and 6.1-m cylinders, shows that there is a significant deviation from the classical cylinder in the cross-flow case. Here, the velocity scale is taken as $U_0 \sin \alpha$, which is appropriate for cross-flow. Each curve represents data for a given cylinder density. In this range of Reynolds numbers based on diameter $4{,}000 < Re_D < 20{,}000$, the drag coefficient values for pure cross-flow range from 1.0 to 1.2 (as published by White 1974), which are approximately two to ten times the values measured in this experiment.

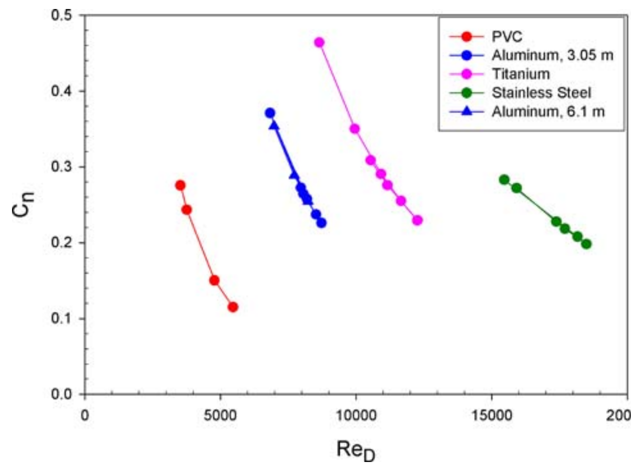

Fig. 15 Orthogonal drag coefficient versus diameter Reynolds number

Not only are the measured values significantly different, but there is a strong dependence on the tow angle, which is inherent in the values of C_n and Re_D, by virtue of the sin α term in each quantity. Figure 16 shows the orthogonal drag force F_γ as a function of tow speed for approximately constant angles. At a given speed, the orthogonal force on the 3.05-m cylinders increases with increasing angle, as expected.

To collapse the data, a scaling is sought for the orthogonal force that takes into account the effect of the turbulent boundary layer in the axial direction. From the data in Fig. 15, it is deduced that the effect of the boundary layer is to reduce the momentum deficit on the low-pressure side (upper surface) of the cylinders, resulting in a lower cross-flow drag. This effect is likely to be accompanied by a marked change in the vortex shedding with respect to the case of simple flow past a cylinder without the presence of an axial boundary layer. An inner variable scaling for the boundary layer is taken to reflect the changes in the cross-flow vortex shedding. The force F_γ is normalized by the corresponding measured axial shear force values, the results of which are shown in Fig. 17. The term $U_0 \sin \alpha / u_\tau$ can be viewed as a Reynolds number based on the viscous length ν / u_τ. The results show that this scaling collapses all data over the range of Reynolds numbers, tow angles, and lengths. Although additional measurements are required to refine this scaling, this analysis provides a simple method to estimate the orthogonal force from the tension (average shear force) and local angle. This approach can be used to improve models of array shape that currently use a single average value for the cross-flow drag coefficient for all angles and speeds.

4 Summary

Direct drag measurements on long, small-diameter towed cylinders at small angles of attack and high Reynolds numbers were performed in the high-speed tow tank at Naval Sea Systems Command (NAVSEA) Carderock. The primary purpose of this investigation was to determine the sensitivity of the tangential drag force to small angles for a long, slender cylinder under tow. The use of a high-speed tow tank enables the development of very high Reynolds number turbulent boundary layers without interference from the walls. The inherent design of the experiment precluded an independent variation of angle and tow speed. A wide range of parameter values was covered during these experiments. The temporal and spatial mean wall shear stress along the cylinder surface was computed from the measured drag, and the data was found to vary from the flat-plate boundary layer case.

The tangential drag coefficient was very sensitive to small changes in tow angle at a given speed. The ratio of the cylinder length to the momentum thickness length scale was used to obtain an improvement in the collapse of the data for all angles and tow speeds in this investigation. While another length scale, such as δ, could provide a tighter collapse of the data, the momentum thickness length scale is readily available in this experiment. Furthermore, it offers an analogy to the flat plate case for which momentum thickness is directly proportional to the drag coefficient. The tangential drag coefficient C_d decreased significantly with increasing speed for all angles tested. Higher angles generally corresponded to larger values of C_d. Also, the values at high speeds are lower than those that flat-plate theories would predict.

As tow speed was increased, the value of $\bar{\tau}_w$ increased to a maximum value and departed significantly from flat-plate values for a range of angles. This trend points to a true Reynolds number effect, and detailed turbulence measurements are required to determine the alteration of the boundary layer structure. The trend of increasing momentum thickness length scale θ with decreasing tow speed and increasing angle was found. At

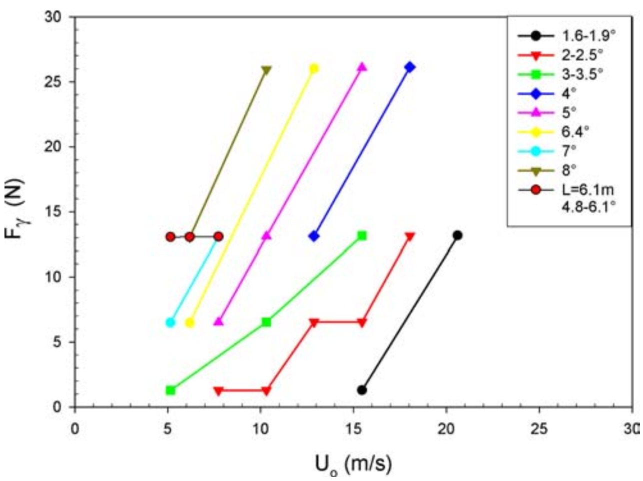

Fig. 16 Orthogonal drag force versus tow speed

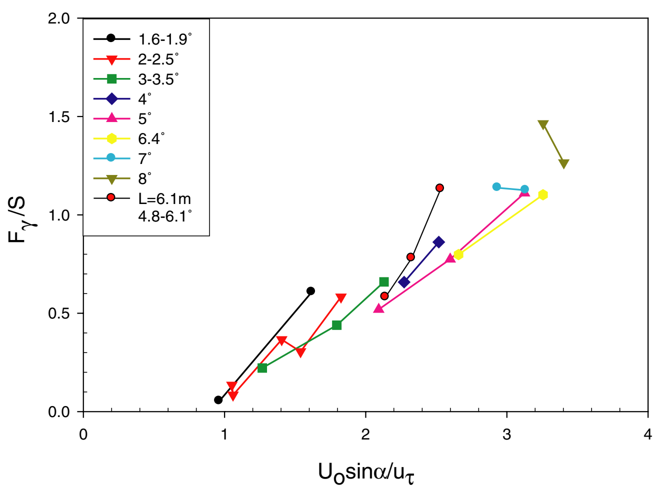

Fig. 17 Orthogonal drag force normalized with shear force

a fixed speed, increasing the tow angle led to an increase in the momentum thickness length scale. The force orthogonal to the cylinder was also computed from the data and was found to be sensitive to tow angle and speed. The related orthogonal drag coefficient is significantly lower than the values for cylinders in pure cross-flow. The measured axial shear force was used to normalize the orthogonal force and to collapse the data for all angles and tow speeds. Additional experiments using cylinders of additional lengths and diameters are required to further refine the scaling laws for the orthogonal force and the tangential drag coefficient.

The results of these experiments confirm that simple corrections to drag forces using components of flow based on geometry are insufficient, which is consistent with the results of Ramberg (1983) and Snarski (2004). The sensitivity of cylindrical boundary layers to small changes in the angle of attack agrees with the findings of Willmarth et al. (1977). For cable dynamics modeling, these results show that applying flat-plate theory to determine the values of the tangential drag coefficients will lead to significant errors. Assumptions for the orthogonal drag based on simple cross-flow, without the presence of a boundary layer, are also inadequate. Future studies should address the sensitivity of the changes in mean wall shear reported by Cipolla and Keith (2003b) to small changes in towing angles.

Acknowledgements The authors wish to acknowledge funding for this effort from the Office of Naval Research codes 321 MS and 333, and the NAVSEA Newport and Carderock In-House Laboratory Independent Research Programs. The authors are grateful to Professor Timothy Wei at Rutgers University for his many helpful discussions.

References

Bucker D, Lueptow RM (1998) The boundary layer on a slightly yawed cylinder. Exp Fluids 25:487–490

Bull MK, Dekkers WA (1993) Vortex shedding from long slender cylinders in near axial flow. Phys Fluids A 5:3296–3298

Cebeci T, Smith AMO (1974) Analysis of turbulent boundary layers. Academic Press, New York, pp 28–32

Cipolla KM, Keith WL (2003a) Momentum thickness measurements for thick axisymmetric turbulent boundary layers. J Fluid Eng 125:569–575

Cipolla KM, Keith WL (2003b) High Reynolds number thick axisymmetric turbulent boundary layer measurements. Exp Fluids 35:477–485

Colella KJ, Keith WL (2003) Measurements and scaling of wall shear stress fluctuations. Exp Fluids 34:253–260

Coles D (1953) Measurements in the boundary layer on a smooth flat plate in supersonic flow, part 1. The problem of the turbulent boundary layer. Report no. 20–69, Jet Propulsion Laboratory, California Institute of Technology Technical Report, Pasadena, California

Fellman MS, Johnston JW (1991) Basin towing evaluations to determine the normal and tangential drag coefficients for four buoyant cable antenna samples. Report no. DTRC-SHD 1357-01, David Taylor Research Center, Bethesda, Maryland

Furey DA, Cipolla KM, Atsavapranee P (2004) Investigation of the turbulent boundary layer flow on a microfilament array. In: Proceedings of the 25th symposium on naval hydrodynamics, St. Johns, Newfoundland, August 2004

Hinze JO (1975) Turbulence, 2nd edn. McGraw-Hill, New York, p 683

Keith WL, Bennett JC Jr (1991) Low frequency spectra of the wall shear stress and wall pressure in a turbulent boundary layer. AIAA J 29:526–530

Kelly HR (1954) A note on the laminar boundary layer on a circular cylinder in axial incompressible flow. J Aeronautical Sci 21:634

Lueptow RM (1988) Turbulent boundary layer on a cylinder in axial flow. Report no. 8389, Naval Underwater Systems Center, New London, Connecticut

Ramberg SE (1983) The effects of yaw and finite length upon the vortex wakes of stationary and vibrating circular cylinders. J Fluid Mech 128:81–107

Schlichting H (1979) Boundary-layer theory, 7th edn. McGraw-Hill, New York, pp 635–667

Schoenherr KE, Brownell WF (1963) The high-speed basin and instrumentation at the David Taylor Model Basin. DTMB Report 1660, January 1963

Snarski SR (2004) Flow over yawed circular cylinders: wall pressure spectra and flow regimes. Phys Fluids 16:344–359

White FM (1969) Axisymmetric turbulent boundary layer on an extremely long cylinder. NUSL report no. 1058, Navy Underwater Sound Lab, New London, Connecticut

White FM (1974) Viscous fluid flow. McGraw-Hill, New York, p 207

Willmarth WW, Winkel RE, Sharma LK, Bogar TJ (1976) Axially symmetric turbulent boundary layers on cylinders: mean velocity profiles and wall pressure fluctuations. J Fluid Mech 76(1):35–64

Willmarth WW, Sharma LK, Inglis S (1977) The effect of cross flow and isolated roughness elements on the boundary layer and wall pressure fluctuations on circular cylinders. Report no. 014439-01, Department of Aerospace Engineering, University of Michigan, Ann Arbor Michigan